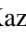



Arbitrary Lagrangian-Eulerian unstructured finite-volume lattice-Boltzmann method for computing two-dimensional compressible inviscid flows over moving bodies

Kazem Hejranfar ^{*}, Hossein Hashemi Nasab, and Mohammad Hadi Azampour
Aerospace Engineering Department, Sharif University of Technology, Tehran 11365-11155, Iran

 (Received 20 March 2019; revised manuscript received 12 December 2019; accepted 23 December 2019; published 18 February 2020)

The objective of this study is to develop and apply an arbitrary Lagrangian-Eulerian unstructured finite-volume lattice-Boltzmann method (ALE-FVLBM) for solving two-dimensional compressible inviscid flows around moving bodies. The two-dimensional compressible form of the LB equation is considered and the resulting LB equation is formulated in the ALE framework on an unstructured body-fitted mesh to correctly model the body shape and properly incorporate the mesh movement due to the body motion. The spatial discretization of the resulting system of equations is performed by a second-order cell-centered finite-volume method on arbitrary quadrilateral meshes and an implicit dual-time stepping method is utilized for the time integration. To stabilize the numerical solution, appropriate numerical dissipation terms are added to the formulation. At first, the shock tube problem is computed to examine the accuracy of the solution obtained by applying the proposed FVLBM for this unsteady test case which includes shock, expansion wave, and contact discontinuity in the flow domain. Then, the stationary isentropic vortex is simulated on both the stationary and moving meshes to assess the implementation of the geometric conservation law in enhancing the solution accuracy of the ALE-FVLBM. The compressible inviscid flow in the transonic regime is then computed around the stationary NACA0012 airfoil in order to further study the sensitivity of the solution method to the user defined parameters. Now, the transonic inviscid flow is simulated over the pitching or plunging NACA0012 airfoil to investigate the accuracy and capability of the proposed solution method (ALE-FVLBM) for the computation of the compressible flows over moving bodies. Finally, the pitching or plunging NACA0012 airfoil near the ground in the transonic inviscid flow is simulated as a practical and challenging problem to study the ground effect on the aerodynamic characteristics of the airfoil. It is indicated that the solution methodology proposed based on the finite-volume LBM formulated in the arbitrary Lagrangian-Eulerian framework (ALE-FVLBM) is capable of accurately computing the compressible inviscid flows around the moving bodies with and without the ground effect.

DOI: [10.1103/PhysRevE.101.023308](https://doi.org/10.1103/PhysRevE.101.023308)

I. INTRODUCTION

In the recent three decades, the lattice-Boltzmann method (LBM) due to its simplicity and genericity has drawn a lot of attention towards itself. The LBM originally developed from the lattice gas cellular automata (LGCA) is a statistical gas kinetic approach which in its discrete form is called the lattice-Boltzmann (LB) equation [1]. The conventional LBM has been used widely in the literature in conjunction with the Bhatnagar-Gross-Krook (BGK) model [2] for the collision term as an alternative to the Euler or Navier-Stokes equations in order to simulate the behavior of the fluid flow. Owing to the advantages of the LBM, several efforts have been made by the researchers to extend the conventional LB formulation and enhance the accuracy and performance of its solution by applying different numerical schemes including the finite-difference [3–9], finite-volume [10–13], finite-element [14–16], spectral collocation [17,18], and spectral difference [19,20] methods and these studies using the LB formulation have been performed for the simulation of the fluid flow around the stationary bodies.

One of the most common challenges in the fluid mechanics engineering is to predict the fluid flow behavior in the neighborhood of moving bodies. Some studies have been performed in the literature to utilize the LBM in order to simulate the fluid flow over the moving bodies using the immersed boundary method (IB-LBM) [21–25] or by applying the bounce-back boundary condition on the Cartesian grids and interpolations (IBB) [26–28]. Dorschner *et al.* [29,30] modified the immersed wall boundary condition for the entropic LBM (ELBM) to reasonably handle complex flow geometries including moving bodies in the incompressible flows. Due to the implementation of the IBM or IBB in these studies, the shape of the body is not correctly modeled, and hence, the wall boundary condition will not be imposed accurately. Note also that these studies are performed by using the standard collision-advection LBM and to lower the computational cost they are based on a coarse background grid for the simulation of the physical domain and a fine grid near the body to improve the accuracy of the solution method there, and this procedure will increase the complexity of the solution method. Di Ilio *et al.* [31–33] proposed a moving grid hybrid LBM (MG-HLBM) to simulate the fluid-solid interaction problems in the incompressible flows. In their method, the

^{*}khejran@sharif.edu

region around the body is solved by using the finite-volume LBM on the unstructured grids and the solution of the outer domain is obtained by the standard single-time relaxation LBM on the structured Cartesian grids and the exchange of the information between these two grids is performed by an interpolation procedure. Meldi *et al.* [34] developed an arbitrary Lagrangian-Eulerian (ALE) form of the LB equation to solve the incompressible flow over the moving bodies. They used two moving and basic grids, a moving grid for describing the flow around the body and an Eulerian frame fixed grid for resolving the physical domain, and an interpolation technique is used for the communication between these two grids. Note that the use of such interpolation procedure between the moving and basic grids is not simple and the results of this solution procedure may be dependent on the utilized interpolation technique. It should be pointed out that the above solution methods are applied to simulate the incompressible flows over the moving bodies.

The objective of the present work is to propose and assess a suitable solution procedure based on the LBM in the ALE framework for simulating the compressible inviscid flows over the moving bodies that does not have the previously mentioned deficiencies. Here, an unstructured finite-volume LBM formulated in the ALE framework is developed and applied to satisfy this goal. Note that the solution of such problems has been extensively carried out in the literature by solving the compressible Euler equations in the ALE form (for example see [35–39]) and the same procedure is adopted here to formulate and apply a finite-volume LBM in the ALE framework on the unstructured meshes. In the proposed ALE unstructured finite-volume lattice-Boltzmann method (FVLBM), the body shape is correctly modeled by using an unstructured body-fitted mesh and the motion of the body is properly made by a suitable unstructured mesh movement strategy. For a compressible thermal fluid flow condition, different LB models have been proposed in the literature (for example see [6,7,40–51]), and here, the multiple particle speeds model proposed by Watari is used. Since a compressible LB formulation is adopted here, the proposed solution method has the capability of simulating the compressible flow field with the discontinuities such as shocks. The use of the finite-volume method to solve the compressible LB equation in the ALE framework on the unstructured meshes provides an appropriate solution methodology to effectively simulate the compressible inviscid flows over practical and challenging problems, as examined in the present study.

In the rest of the paper, the compressible LBM in the ALE framework is introduced, the discretization of the resulting system of equations both spatially and temporally by using the finite-volume method is given, and the strategy of the unstructured mesh movement is described. Then, the proposed solution method (ALE-FVLBM) is applied to simulate several test cases, including the shock tube, the stationary isentropic vortex on both the stationary and moving meshes, the stationary, pitching, or plunging NACA0012 airfoil in the transonic inviscid regime, and, as a more practical and challenging test case, the ground effect on the flow field near the pitching or plunging NACA0012 airfoil in the transonic inviscid regime is also investigated. Finally, some conclusions and remarks are given.

II. GOVERNING EQUATION; COMPRESSIBLE LB FORMULATION IN ALE FRAMEWORK

In the present study, the LB equation with a single relaxation time Bhatnagar-Gross-Krook (BGK) model [2] for the collision term is used as the governing equation for the simulation of compressible flows as follows:

$$\frac{\partial f_{kl}}{\partial t} + (\mathbf{c}_{kl} \cdot \nabla) f_{kl} = -\frac{1}{\tau} (f_{kl} - f_{kl}^{\text{eq}}), \quad (1)$$

which in the ALE form becomes

$$\frac{\partial f_{kl}}{\partial t} + [(\mathbf{c}_{kl} - \dot{\mathbf{r}}) \cdot \nabla] f_{kl} = -\frac{1}{\tau} (f_{kl} - f_{kl}^{\text{eq}}), \quad (2)$$

where t is the time, τ is the collision relaxation time, f_{kl}^{eq} is the equilibrium distribution function, and \mathbf{c}_{kl} is the particle velocity vector. The subscripts k and l indicate a group of particles with the translational velocity c_k and the direction of particle, respectively. In Eq. (2), $\dot{\mathbf{r}} = (\dot{x}, \dot{y})$ represents the grid velocity vector and knowing that $\dot{\mathbf{r}}$ is a solenoidal field, the convection term in this equation can be written in the conservative form as

$$\frac{\partial f_{kl}}{\partial t} + \nabla \cdot \mathbf{H}(f_{kl}) = -\frac{1}{\tau} (f_{kl} - f_{kl}^{\text{eq}}), \quad (3)$$

where $\mathbf{H}(f_{kl})$ is the total flux density of f_{kl} and it can be described as

$$\mathbf{H}(f_{kl}) = (\mathbf{c}_{kl} - \dot{\mathbf{r}}) f_{kl} = (c_{kl_\alpha} - \dot{r}_\alpha) f_{kl} \hat{e}_\alpha, \quad \alpha = 1, 2, \quad (4)$$

and this formulation written in the ALE form is suitable for the discretization by using the finite-volume method on moving meshes applied in the present study to solve the compressible inviscid flows over moving bodies.

To correctly model the compressibility in a thermal fluid flow, one should use multiple particle speeds, and here, the two-dimensional compressible LB model proposed by Watari [6,7] is used. In this LB model, the macroscopic properties of the fluid flow are calculated by the following relations:

$$\rho = \sum_k \sum_l f_{kl}, \quad \rho \mathbf{u} = \sum_k \sum_l f_{kl} \mathbf{c}_{kl},$$

$$\rho \left(\frac{D+n}{D} e + \frac{\mathbf{u} \cdot \mathbf{u}}{2} \right) = \sum_k \sum_l f_{kl} \left(\frac{c_k^2}{2} + \frac{\eta_k^2}{2} \right), \quad (5)$$

TABLE I. Particle velocities and extra energy speeds of 2D Watari LB model [7].

k : group	l : direction	c_k	η_k
0	1	$c_0 = 0$	$\eta_0 = 0$
1	1–8	$c_1 = 1$	$\eta_1 = 1$
2	1–8	$c_2 = 2$	$\eta_2 = 2$
3	1–8	$c_3 = 3$	$\eta_3 = 3$
4	1–8	$c_4 = 4$	$\eta_4 = 4$
5	1–8	$c_5 = c_1 = 1$	$\eta_5 = 0$
6	1–8	$c_6 = c_2 = 2$	$\eta_6 = 0$
7	1–8	$c_7 = c_3 = 3$	$\eta_7 = 0$
8	1–8	$c_8 = c_4 = 4$	$\eta_8 = 0$

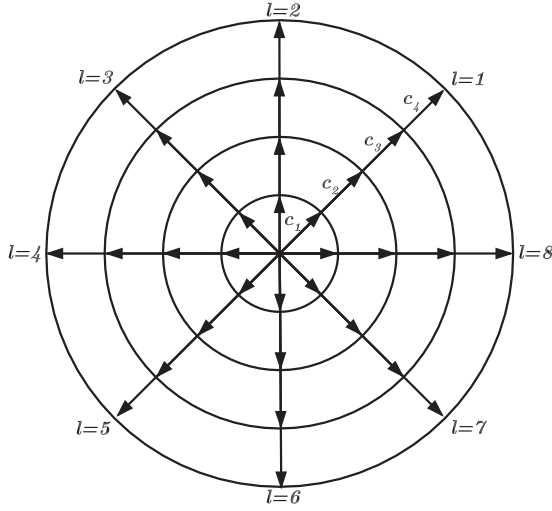


FIG. 1. Particle velocities in two-dimensional (2D) LB model proposed by Watari [7].

where D indicates the number of spatial dimensions and n represents the number of extra degrees of freedom with the

energy level of $\eta_k^2/2$ according to the translation or rotation. In the Watari model, 65 particle velocities divided in nine groups are used, including the particle at rest ($k = 0$) and two other classes, each containing four groups of the octagon particles, one with an extra degree of freedom ($k = 1-4$) and the other with no extra degrees of freedom ($k = 5-8$), as given in Table I and Fig. 1, illustrates a class consisting 32 of the particle velocities.

The total internal energy E in this LB model can be calculated as

$$E = \frac{D+n}{D}e, \quad (6)$$

where the translational internal energy e , the pressure p , the temperature T , and the specific-heat ratios γ are calculated by

$$p = \frac{2}{D}\rho e, \quad T = \frac{2}{D}e, \quad \gamma = \frac{D+n+2}{D+n}. \quad (7)$$

The Watari model is capable of modeling the fluid flow with different specific-heat ratios and, in the current study, both the ideal monatomic ($D = 2$, $n = 1$, $\gamma = 5/3$) and diatomic ($D = 2$, $n = 3$, $\gamma = 7/5$) gasses are considered. In the Watari model, the local equilibrium distribution function is given by

$$f_{kl}^{\text{eq}} = \rho F_k \left[\left(1 - \frac{\mathbf{u} \cdot \mathbf{u}}{2e} + \frac{(\mathbf{u} \cdot \mathbf{u})^2}{8e^2} \right) + \frac{1}{e} \left(1 - \frac{\mathbf{u} \cdot \mathbf{u}}{2e} \right) (\mathbf{c}_{kl} \cdot \mathbf{u}) + \frac{1}{2e^2} \left(1 - \frac{\mathbf{u} \cdot \mathbf{u}}{2e} \right) (\mathbf{c}_{kl} \cdot \mathbf{u})^2 + \frac{1}{6e^3} (\mathbf{c}_{kl} \cdot \mathbf{u})^3 + \frac{1}{24e^4} (\mathbf{c}_{kl} \cdot \mathbf{u})^4 \right], \quad (8)$$

where F_k is the weighting coefficient and it is obtained as

$$F_k = \begin{cases} 1 - 8(F_1 + F_2 + F_3 + F_4 + F_5 + F_6 + F_7 + F_8), & k = 0 \\ \frac{\frac{n}{\eta_k^2} (6e^4 - e^3 \sum_i^{i \neq k} c_i^2 + \frac{1}{8} e^2 \sum_i^{i \neq k} \sum_j^{i \neq k, j \neq k} (c_i c_j)^2 - \frac{1}{8} e \Pi_i^{i \neq k} c_i^2)}{\Pi_i^{i \neq k} (c_i^2 - c_i^2)}, & k = 1, 2, 3, 4 \\ \frac{48e^4 - 6e^3 \sum_i^{i \neq k} c_i^2 + \frac{1}{2} e^2 \sum_i^{i \neq k} \sum_j^{i \neq k, j \neq k} (c_i c_j)^2 - \frac{1}{4} e \Pi_i^{i \neq k} c_i^2}{\Pi_i^{i \neq k} (c_i^2 - c_i^2)}, & k = 5, 6, 7, 8 \end{cases} \quad (9)$$

It is noteworthy that all the variables in the aforementioned equations are in a dimensionless form as follows:

$$\begin{aligned} \mathbf{r} &= \frac{\mathbf{r}^*}{L^*}, & t &= \frac{t^*}{L^*/\sqrt{R^*T_0^*}}, & \tau &= \frac{\tau^*}{L^*/\sqrt{R^*T_0^*}}, & \mathbf{u} &= \frac{\mathbf{u}^*}{\sqrt{R^*T_0^*}}, \\ f_{kl} &= \frac{f_{kl}^*}{\rho_0^*}, & \mathbf{c}_{kl} &= \frac{\mathbf{c}_{kl}^*}{\sqrt{R^*T_0^*}}, & \eta_k &= \frac{\eta_k^*}{\sqrt{R^*T_0^*}}, \\ \rho &= \frac{\rho^*}{\rho_0^*}, & p &= \frac{p^*}{\rho_0^* R^* T_0^*}, & T &= \frac{T^*}{T_0^*}, & e &= \frac{e^*}{R^* T_0^*}, & E &= \frac{E^*}{R^* T_0^*}, \end{aligned} \quad (10)$$

where the superscript $*$ indicates the dimensional variables, the subscript 0 denotes the freestream condition, L represents the reference length, and R^* is the ideal gas constant, respectively.

III. NUMERICAL SOLUTION PROCEDURE

Here, a second-order cell-centered finite-volume method is used for the discretization of the ALE-LB equation (3) on the unstructured meshes. Integrating this equation over the domain Ω confined with its boundary $\partial\Omega$ will result in the following formula:

$$\frac{\partial}{\partial t} \iint_{\Omega} f_{kl} dA + \oint_{\partial\Omega} \mathbf{H}(f_{kl}) \cdot \hat{\mathbf{n}} ds = \iint_{\Omega} -\frac{1}{\tau} (f_{kl} - f_{kl}^{\text{eq}}) dA. \quad (11)$$

Assuming the domain Ω is covered with a finite number of nonoverlapping quadrilateral cells, one can write this equation for each cell as

$$\frac{d}{dt}[(f_{kl})_j A_j] + \underbrace{\sum_{m=1}^{n_{\text{faces}}} \mathbf{H}_m \cdot \hat{\mathbf{n}}_m ds_m}_{R_j(f_{kl})} + \frac{1}{\tau} [(f_{kl})_j - (f_{kl}^{\text{eq}})_j] A_j = 0, \quad (12)$$

where A_j is the area of the cell j , n_{faces} is its number of faces (here, $n_{\text{faces}} = 4$), and $\hat{\mathbf{n}}_m$ is the normal vector to the face m , ds_m is the length of the face m , and \mathbf{H}_m is the flux passing through the face m (see Fig. 2). To calculate the value of the flux at each cell face, a central averaging scheme is used as

$$\mathbf{H}_m = \frac{\mathbf{H}_L + \mathbf{H}_R}{2}, \quad (13)$$

where the subscripts L and R denote the left and right neighboring cell center values of the flux, respectively, and they are calculated by

$$\mathbf{H}_{L,R} = (\mathbf{c}_{kl} - \dot{\mathbf{r}})_{L,R}(f_{kl})_{L,R}. \quad (14)$$

A. Dissipation terms

In order to reduce the effect of the Gibbs phenomenon caused by the odd-even decoupling as a result of the form of the spatial discretization used here and to reasonably capture the discontinuities in the flow field such as shocks, the numerical dissipation term $D(f_{kl})$ is added to Eq. (12) as

$$\frac{d}{dt}[(f_{kl})_j A_j] + R(f_{kl})_j - D(f_{kl})_j = 0, \quad (15)$$

where

$$D(f_{kl})_j = \sum_{m=1}^N (d_{kl})_{ij}, \quad (16)$$

in which N is the number of cells connected to the j th cell and $(d_{kl})_{ij}$ is the dissipation on the interface of the j th cell

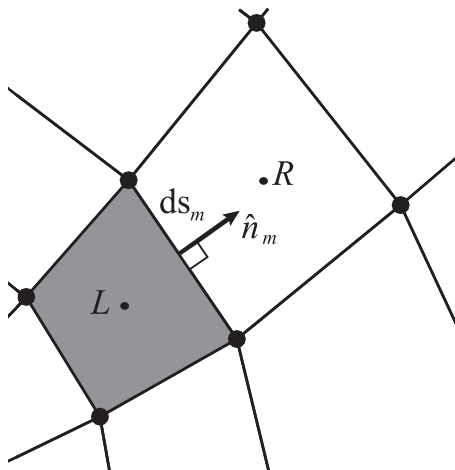


FIG. 2. A schematic of computational quadrilateral mesh.

and the neighboring cell i on its m th face. Note that $(d_{kl})_{ij}$ is composed of two parts of the second- and fourth-order dissipation terms. The former is used to damp the oscillations near the discontinuities in the solution domain and the latter is used to eliminate the high-frequency oscillations raised from the odd-even decoupling, and thus $(d_{kl})_{ij}$ is calculated as

$$(d_{kl})_{ij} = \lambda_{ij} \{ \varepsilon_{ij}^{(4)} [\nabla^2(f_{kl})_j - \nabla^2(f_{kl})_i] - \varepsilon_{ij}^{(2)} [(f_{kl})_j - (f_{kl})_i] \}, \quad (17)$$

where

$$\nabla^2(f_{kl})_j = \sum_{m=1}^N [(f_{kl})_i - (f_{kl})_j] \quad (18)$$

and the other variables are calculated as

$$\lambda_{ij} = \frac{1}{2} \left(\frac{A_j}{\Delta t_j} + \frac{A_i}{\Delta t_i} \right), \quad v_j = \sum_{k=1}^N \frac{|p_j - p_k|}{(p_j + p_k)},$$

$$\varepsilon_{ij}^{(2)} = k_2 \max(v_j, v_i), \quad \varepsilon_{ij}^{(4)} = k_4 \max(0, k_4 - \varepsilon_{ij}^{(2)}), \quad (19)$$

where in the above relations, the index j represents the target cell and the index i indicates its neighbors. The sensor v_i works in such a way that near the discontinuities in the solution domain the fourth-order dissipation term will not be activated and only the second-order dissipation term will be activated, as explained before. The coefficients k_2 and k_4 are two user defined parameters adjusting the intensity of the second- and fourth-order dissipation terms, respectively. The formulation of the numerical dissipation terms given here to be used for the solution of the compressible LB equation is nearly similar to that applied for the solution of the compressible Euler equations [39,52].

B. Boundary conditions

In the present study, different types of boundary conditions (BCs) are encountered including the slip wall, inflow, and outflow BCs. Here, the fictitious cell approach is applied in which each boundary cell has a fictitious cell in the neighboring of its boundary face. To calculate the distribution function f_{kl} on these fictitious cells, the boundary conditions are treated for both the mesoscopic and macroscopic scales. In the macroscopic scale, the flow tangency condition on the wall boundary is used for the stationary or moving body considering the simulations performed under the inviscid flow assumption to calculate the velocity components (u, v) in each wall fictitious cell. The pressure and density variables in that wall fictitious cell are calculated by setting $\partial p / \partial n = 0$ and $\partial \rho / \partial n = 0$ on the wall boundary (where n is the direction normal to the

wall). For the far-field boundary, the nonreflecting (characteristic) boundary conditions are used [39,53] to calculate the velocity components and the density and pressure variables in each far-field fictitious cell.

In the mesoscopic scale, the nonequilibrium distribution function f_{kl}^{neq} in each fictitious cell is calculated in which its second derivative $\partial^2 f_{kl}^{\text{neq}}/\partial n^2$ is set to be vanished on the corresponding boundary face. In the next step, in order to calculate the LB distribution function f_{kl} on each fictitious cell, the equilibrium distribution function calculated from the macroscopic scale variables using Eq. (8) and the nonequilibrium distribution function obtained from the mesoscopic scale are added together on that fictitious cell, i.e., $f_{kl} = f_{kl}^{\text{eq}} + f_{kl}^{\text{neq}}$. In this procedure, considering that all the variables are calculated on the center of the numerical cells, no population will be lost.

C. Time integration scheme

Here, the time integration is efficiently performed by applying an implicit dual-time stepping method [20] and it is made by adding a pseudotime derivative term to Eq. (15) as follows:

$$A_j^{n+1} \frac{\partial (f_{kl})_j^{n+1}}{\partial \tilde{\tau}} + R^*[(f_{kl})_j^{n+1}] = 0, \quad (20)$$

where n is the real time-step level, $\tilde{\tau}$ represents the pseudotime, and $R^*(\cdot)$ indicates the residual in the pseudotime level and the discretization of the real time by using the second-order backward differencing will result in

$$R^*[(f_{kl})_j^{n+1}] = \frac{3A_j^{n+1}(f_{kl})_j^{n+1} - 4A_j^n(f_{kl})_j^n + A_j^{n-1}(f_{kl})_j^{n-1}}{2\Delta t} + R[(f_{kl})_j^{n+1}] - D[(f_{kl})_j^{n+1}]. \quad (21)$$

Note that the time integration for the solution of Eq. (20) in the pseudotime level can be performed by either low- or high-order explicit schemes. Since the accuracy of the time integration in the pseudotime level is not important, a simple explicit scheme is used here. To calculate f_{kl}^{n+1} at the new real time level $n+1$, Eq. (20) is solved iteratively in the pseudotime τ and the iteration procedure will be continued to reach the specified convergence criterion considered.

D. Mesh movement strategy and geometric conservation law

The fluid flow problems that include moving boundaries are very common and can be simulated via a suitable mesh movement strategy. Here, the linear spring analogy proposed by Batina [35] is adopted for this aim. In this method, at each time step the new coordinates of the mesh nodes are calculated using their previous locations, and therefore, the data structure remains intact. To perform the linear spring method, each edge of a cell is presumed as a tensile spring; somehow the stiffness of the fictitious spring increases as the length of the edge decreases. Therefore, for the edge that connects the nodes p and q , the stiffness C_{pq} of the adjacent spring is calculated by

$$C_{pq} = \frac{1}{l_{pq}^2} = \frac{1}{|\mathbf{r}_p - \mathbf{r}_q|^2}. \quad (22)$$

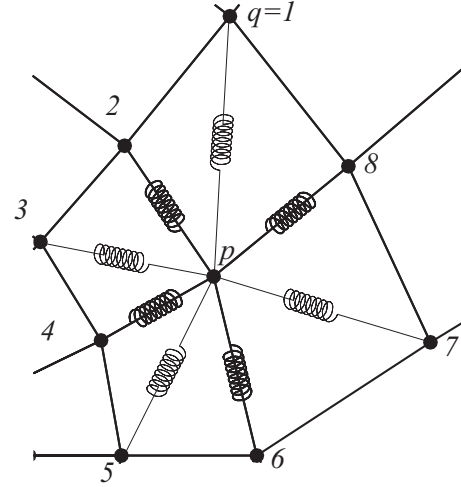


FIG. 3. A schematic of spring network used.

When a small motion happens in a boundary of the solution domain, the following equations are solved in an iterative manner until all the nodes reach an equilibrium from the perspective of the second law of Newton:

$$\Delta \mathbf{r}_p^{n+1} = \frac{\sum_q C_{pq} \Delta \mathbf{r}_q^n}{\sum_q C_{pq}}, \quad (23)$$

where p is the target node and q represents any node connected to the target node through a real or virtual connection (see Fig. 3). Note that this traditional formulation of the linear spring does not model a network of springs because the two coordinates in Eq. (23) are decoupled. It means that any deformation in one direction would result in the displacement of the nodes in that direction only. To overcome this difficulty of the traditional form of the linear springs, Farhat [54] proposed a modified formulation of the linear springs in which a real network of springs would be modeled and this technique is adopted in the present study. Although the modified linear spring can handle the problems with relatively large displacements, such conditions are not considered for the moving NACA0012 airfoil studied here in the pitching or plunging motions. Note that inviscid flow computations over the NACA0012 airfoil with large displacements do not provide physical results because of the occurrence of the separated flows due to the viscous effects, which are neglected in the present study, and for providing the physical results for these conditions, the ALE-FVLBM should be extended to consider the viscous effects.

The deformation of the computational cells due to moving boundaries will change the area of each cell and according to the formulation, the calculation of each cell area is required in every time step. Given that the mesh motion algorithm is solved approximately, if one computes the area of a cell using the coordinates of its vertices, the solution may encounter an error over the time. To avoid such error, the geometric conservation law (GCL) should be used in which the area of each cell is integrated forward in the time using the same numerical scheme applied to the governing equations [55]. Here, the GCL is implemented by considering the ALE-LB

equation (11) reformulated as follows:

$$\frac{\partial}{\partial t} \iint_{\Omega} dA - \oint_{\partial\Omega} \dot{\mathbf{r}} \cdot \hat{\mathbf{n}} dS = 0, \quad (24)$$

where the parameters involved in this equation have been introduced before. Using the second-order time discretization, Eq. (24) becomes

$$A^{n+1} = \frac{4A^n - A^{n-1} + 2\Delta t \theta^{n+1}}{3} \quad (25)$$

in which

$$\theta^{n+1} = \sum_{m=1}^4 [(\dot{x} \hat{n}_x + \dot{y} \hat{n}_y)_m dS_m]. \quad (26)$$

The effect of the implementation of the GCL on the solution of the ALE-FVLBM will be investigated in the present study by simulating the stationary isentropic vortex problem on the moving meshes.

IV. RESULTS AND DISCUSSION

The present solution methodology based on the application of the second-order cell-centered finite-volume LBM in the ALE framework (ALE-FVLBM) on the unstructured meshes is assessed by simulating different compressible inviscid flows. At first, the Sod shock tube problem is simulated by applying the proposed FVLBM and the present solution is compared with the exact solution for this Riemann problem. Then, to evaluate the effects of the implementation of the GCL on the solution of the ALE-FVLBM, the stationary isentropic vortex is simulated on both the stationary and moving meshes. The simulation of the compressible inviscid flow over the stationary, pitching, or plunging NACA0012 airfoil is then carried out by applying the ALE-FVLBM on the quadrilateral meshes and the present results are compared to the available numerical and experimental ones. As a practical and challenging problem, the pitching or plunging NACA0012 airfoil in the presence of a wall, to replicate the ground effect, is also simulated. All the simulations performed in the present study are carried out for the diatomic ideal gas, $\gamma = 7/5$, unless otherwise specified.

All the simulations performed here are carried out on a computer with the following specifications: Core i7-3.4 GHz CPU with 16-GB RAM. A typical computational time based on the wall clock required for the simulation of the compressible inviscid flow over the moving NACA0012 airfoil for 1000 iterations is about 12 sec. The parallel processing is not implemented here, however, it is possible to do so according to the compatibility of the LBM with the parallel algorithms to reduce the computation time needed.

A. Sod shock tube

To investigate the ability of the present solution method to resolve the discontinuities in the solution domain, the Sod shock tube problem is simulated here. The solution starts from

the following initial condition:

$$(\rho, u, p) = \begin{cases} (1, 0, 1), & x \leq 0.5 \\ (0.125, 0, 0.1), & x > 0.5 \end{cases} \quad (27)$$

and the present results by applying the proposed FVLBM are compared to the exact solution at the time $t = 0.2$. The solution domain is extended from $x = 0$ to $x = 1$ and from $y = 0$ to $y = 0.06$ and covered with 1000×6 uniform quadrilateral cells in the x and y direction, respectively. Here, the periodic condition is used for the upper and lower boundaries and the extrapolation is applied for the left and right sides of the solution domain to calculate the particle distribution function f_{kl} on the boundaries. The real time step size considered in the dual-time stepping method for computing the shock tube problem using the proposed FVLBM is set to be $\Delta t = 0.0001$.

A sensitivity study is made to study the effects of the numerical parameters on the solution of the FVLBM applied. Similar to the study performed in Ref. [20], the present study has shown that the value of the relaxation time τ can affect the inviscid solution of the FVLBM applied and its value should be selected as small as possible to obtain more accurate solution with a low level of oscillations. Here, the value of the relaxation time is selected to be $\tau = 0.0001$ and the results show that it provides a reasonable solution in comparison with the exact solution for the shock tube problem. Now, the effect of the values of the second- and fourth-order dissipation coefficients on the solution of the FVLBM applied is investigated, as shown in Fig. 4. The study shows that the numerical dissipation terms implemented in the solution algorithm of the FVLBM can have significant effects on the solution. It is indicated that the solution near the discontinuities is smeared by increasing the values of the numerical dissipation coefficients and some oscillations are observed by decreasing them, and the study shows that $k_2 = 0.125$ and $k_4 = 0.002$ are suitable to obtain a reasonable solution compared to the exact solution. The convergence history of the solution obtained by applying the proposed dual-time stepping FVLBM for the shock tube problem is given in Fig. 5 which indicates the solution is reasonably converged in the pseudotime level for each real time step size.

Given that the proposed FVLBM with incorporating the Watari model in the formulation can consider different values of the specific-heat ratios, the present simulations are performed for both the diatomic and monatomic ideal gases, $\gamma = 7/3$ and $\gamma = 5/3$. Figure 6 shows a comparison of the solution obtained by the FVLBM applied for both the ideal gases and good agreement is observed in comparison with the exact solution for both cases.

B. Stationary isentropic vortex

The simulation of the stationary isentropic vortex on the stationary or moving meshes is performed here to assess the effect of implementing the GCL on enhancing the accuracy of the solution of the proposed ALE-FVLBM. The computational domain is a 10×10 square and the macroscopic variables are initialized as $(\rho, u, v, p) = (1, 0, 0, 1)$, and then, the isentropic vortex is added to the mean flow

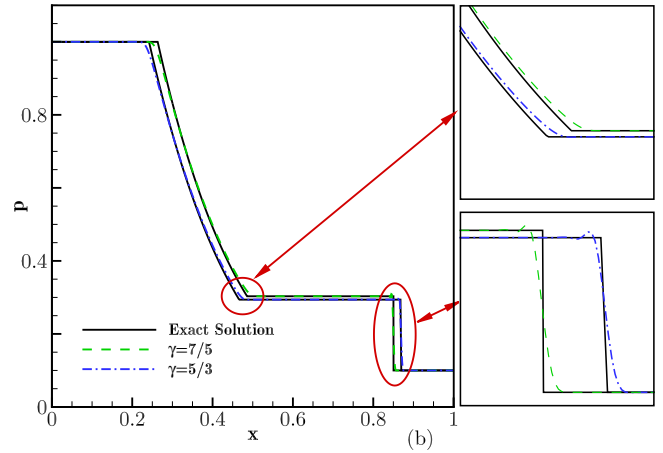
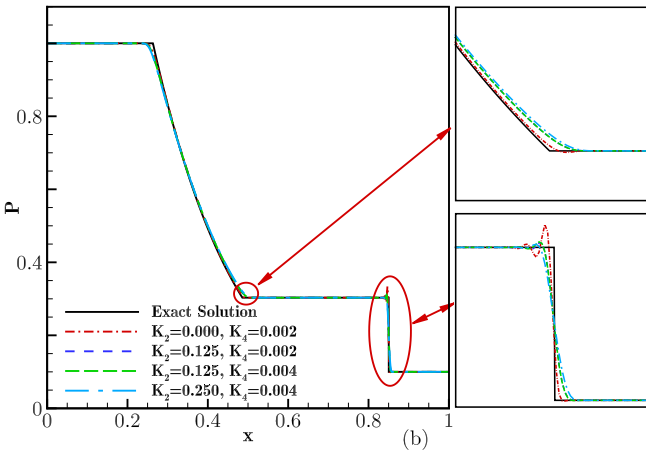
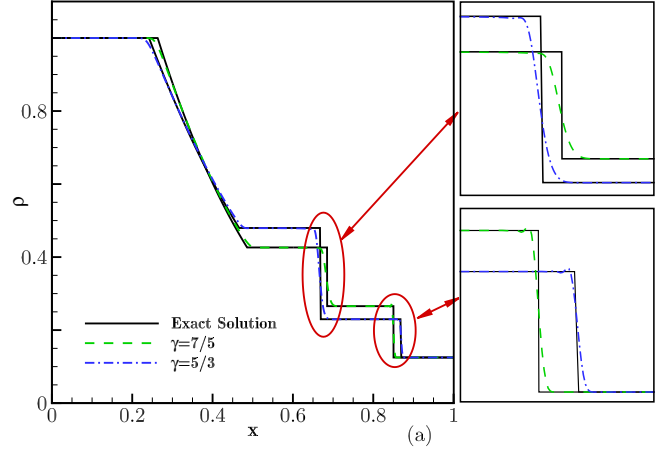
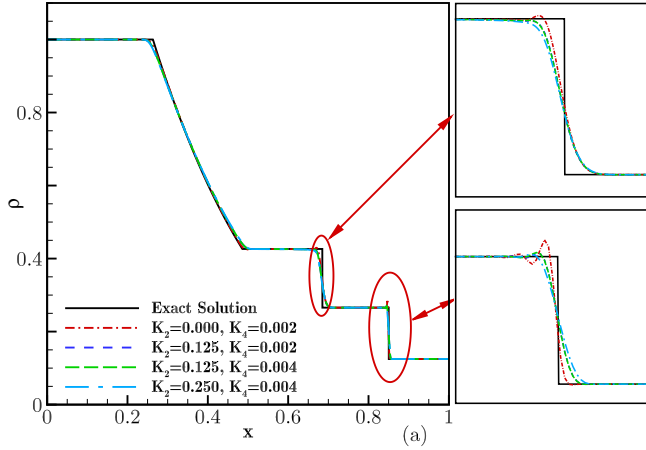


FIG. 4. Effect of value of dissipation coefficients on distribution of (a) density and (b) pressure for the shock tube problem.

FIG. 6. Comparison of distribution of (a) density and (b) pressure for the shock tube problem for $\gamma = 7/5$ and $\gamma = 5/3$.

with perturbations in the velocities and no perturbation in the entropy as follows:

$$(\delta u, \delta v) = \epsilon \kappa e^{\alpha(1-\kappa^2)} (-\sin \tilde{\theta}, \cos \tilde{\theta}), \quad \delta s = 0, \quad (28)$$

where the density and the pressure are obtained by

$$\rho = \left(1 - \frac{(\gamma - 1)\epsilon^2 e^{2\alpha(1-\kappa^2)}}{4\alpha\gamma} \right)^{1/(\gamma-1)}, \quad p = \rho^\gamma. \quad (29)$$

In the above relations, $\tilde{\theta}$ is the angle of each point with respect to the positive x axis while the origin is set to be the center of the vortex $(x_c, y_c) = (5, 5)$. Also, ϵ is the vortex strength, α is the decay rate of the vortex, and $\kappa = r/r_c$, $r = \sqrt{(x - x_c)^2 + (y - y_c)^2}$, in which r_c is the core radius of the vortex and $\epsilon = 5/2\pi$, $\alpha = 0.5$, and $r_c = 1$ are used here. The mesh is forced to move in time according to

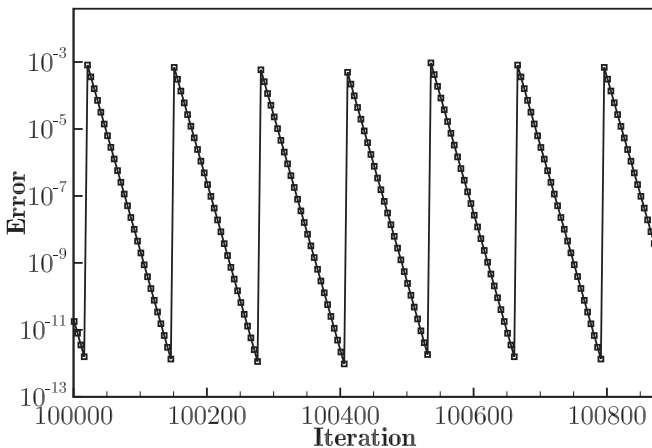


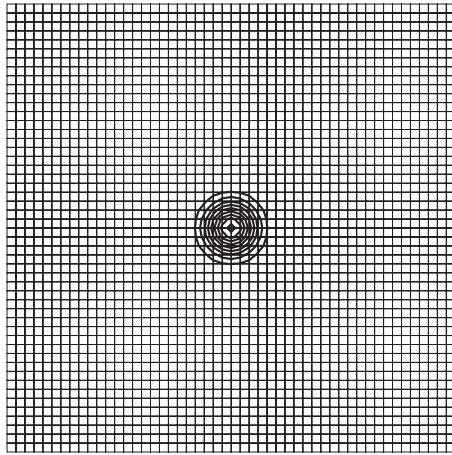
FIG. 5. Convergence history of the solution for the shock tube problem.

$$\begin{aligned} x(t) &= x^r + 2.0 \sin\left(\frac{\pi x^r}{10}\right) \sin\left(\frac{\pi y^r}{10}\right) \sin\left(\frac{2\pi t}{t_0}\right), \\ y(t) &= y^r + 1.5 \sin\left(\frac{\pi x^r}{10}\right) \sin\left(\frac{\pi y^r}{10}\right) \sin\left(\frac{4\pi t}{t_0}\right), \end{aligned} \quad (30)$$

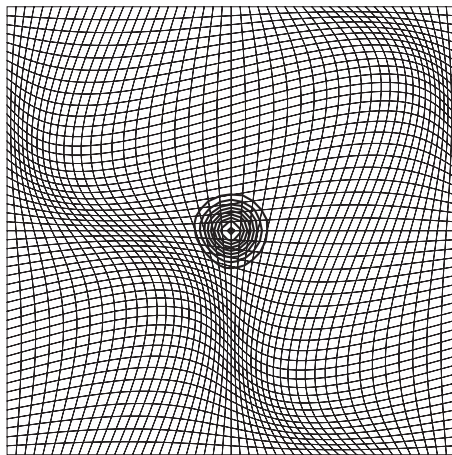
where $t_0 = 1$ is considered and x^r and y^r are the initial coordinates of the mesh at $t = 0$. The periodic condition for the distribution function f_{kl} is applied for all the sides of the solution domain.

Here, the solution is marched in the real time t by using the dual-time stepping method implemented in the ALE-FVLBM and the results for both the stationary and moving meshes

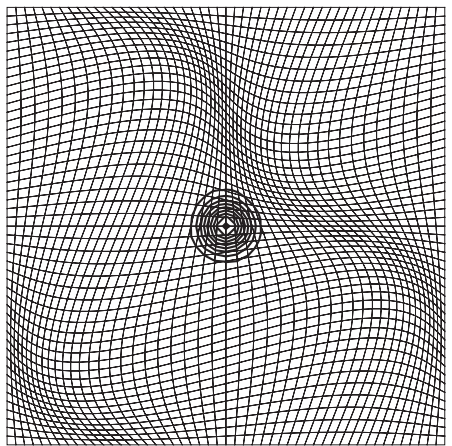
are obtained up to the time $t = 1$ by considering the real time step size $\Delta t = 0.001$. The value of the relaxation time for this investigation is considered to be small, i.e., $\tau = 0.0001$, to reasonably represent an inviscid calculation. Now,



(a)



(b)



(c)

FIG. 7. Moving mesh and computed flow field shown by density contours for three different times of the solution, (a) $t = 0$, (b) $t = 0.25$, (c) $t = 0.75$, for the isentropic vortex problem.

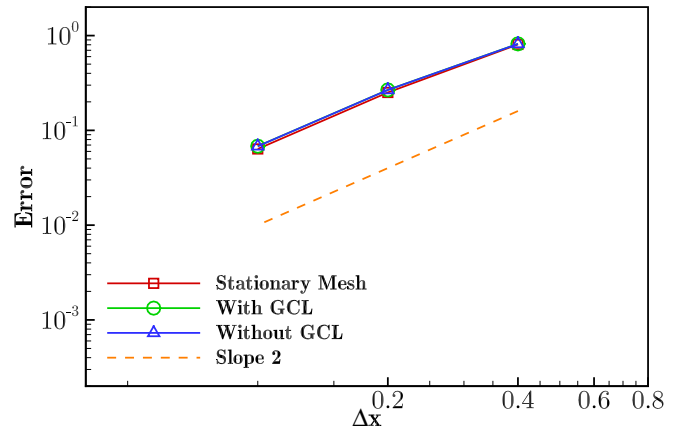


FIG. 8. Order of spatial accuracy of the solution for the stationary and moving meshes for the isentropic vortex problem.

the effect of the implementation of the GCL on the spatial and temporal accuracy of the solution of the ALE-FVLBM is examined. To verify the spatial accuracy of the solution, the computations are performed on four different meshes with 2500, 10000, 40000, and 160000 quadrilateral cells and the solution of the finest mesh is considered as the reference solution and the error is calculated based on the L_2 norm of the density for the other meshes compared to the finest one. This investigation is performed for both the stationary and moving meshes and the solution is obtained with and without implementing the GCL for the moving mesh case. The mesh and the computed flow field shown by the density contours for three different times of the solution, $t = 0, 0.25$, and 0.75 , for the moving mesh case are depicted in Fig. 7. The solution for the coarse mesh with 2500 quadrilateral cells is shown here for the mesh movement and the computed flow field to be clearly observed. Figure 8 verifies the second-order spatial accuracy of the present solution method for both the stationary and moving meshes. It is also observed that the implementation of the GCL for the moving mesh case does not have a noticeable effect on the accuracy of the solution of the ALE-FVLBM and the solutions of the stationary and moving

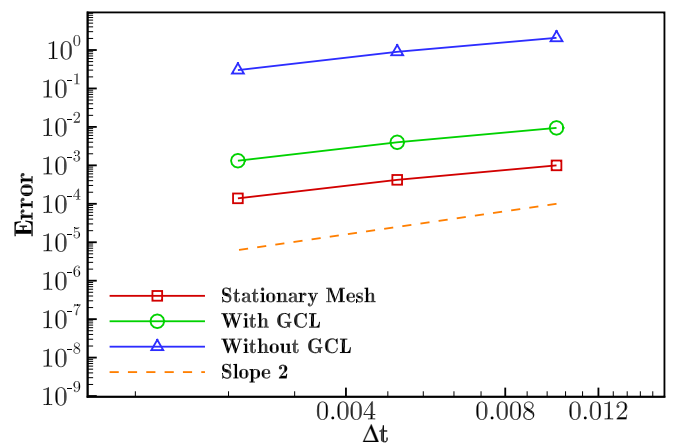


FIG. 9. Order of temporal accuracy of the solution for the stationary and moving meshes for the isentropic vortex problem.

meshes are nearly the same. Now, to investigate the temporal accuracy of the solution of the ALE-FVLBM, four different values for the real time step size are considered, $\Delta t = 0.01, 0.005, 0.0025,$ and $0.00125,$ and the error for each simulation is calculated based on the L_2 norm of the density compared to the reference solution obtained by $\Delta t = 0.00125.$ The simulations are performed for three different conditions: the moving mesh with and without implementing the GCL and the stationary mesh. The second-order temporal accuracy of the solution method adopted is verified for both the stationary and moving meshes, as illustrated in Fig. 9. It is indicated that the implementation of the GCL improves the temporal

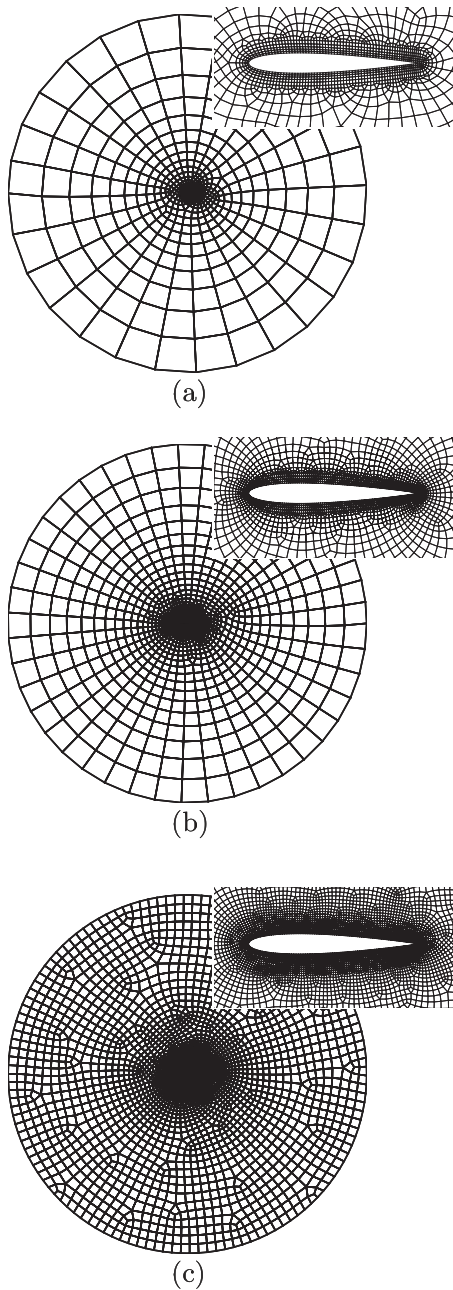


FIG. 10. Unstructured quadrilateral meshes used for the solution of the NACA0012 airfoil; (a) Mesh-I, (b) Mesh-II, and (c) Mesh-III meshes.

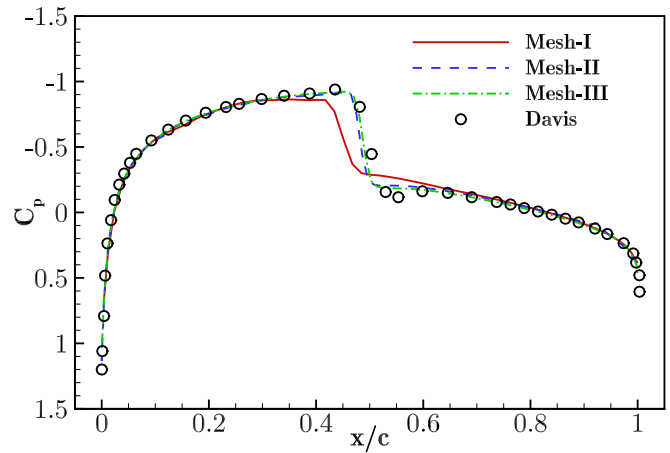


FIG. 11. Effect of grid size on surface pressure coefficient distribution for the stationary NACA0012 airfoil at $\alpha = 0^\circ$ and $M_\infty = 0.8.$

accuracy of the solution of the ALE-FVLBM compared to the solution of the stationary mesh. The trend found by implementing the GCL in the formulation of the ALE-FVLBM is consistent with the study performed for the solution of the Euler equations on the moving meshes in Ref. [56].

C. Stationary NACA0012 airfoil

This test case is concerned with the computation of the steady inviscid transonic flow around the stationary NACA0012 airfoil at $M_\infty = 0.8$ and 0° angle of attack and the present solution by applying the unstructured FVLBM is compared with that of Davis and Bendiksen [38]. This condition is designed to evaluate the ability of the present solution method to capture the discontinuities in the flow field. A sensitivity study is also performed to examine the effects of the numerical parameters including the mesh size and the values of the numerical dissipation coefficients on the accuracy of the steady solution obtained by the unstructured FVLBM applied. Here, the steady solution is obtained by

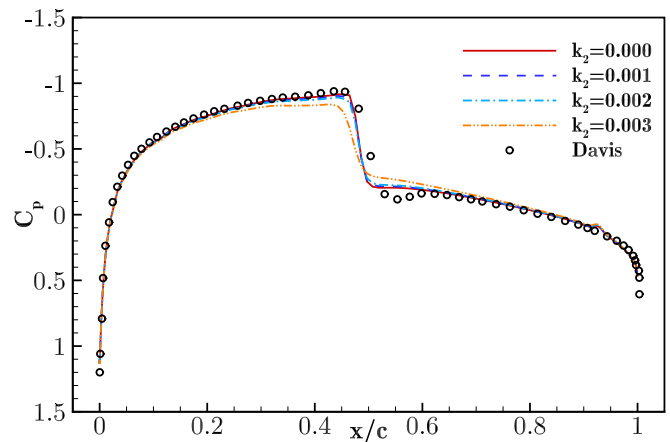


FIG. 12. Effect of value of second-order dissipation coefficient on surface pressure coefficient distribution for the stationary NACA0012 airfoil at $\alpha = 0^\circ$ and $M_\infty = 0.8.$

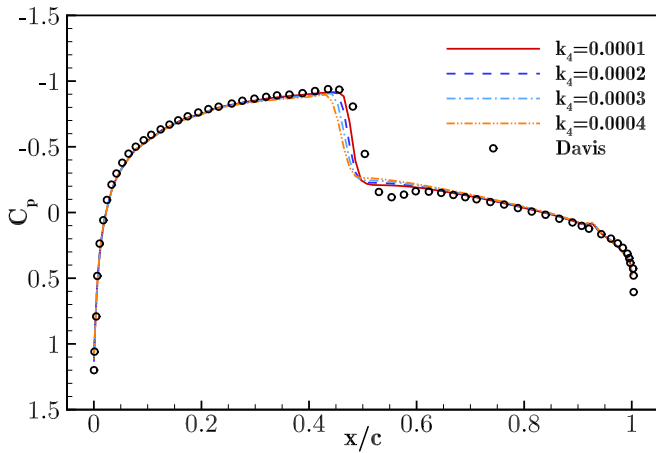


FIG. 13. Effect of value of fourth-order dissipation coefficient on surface pressure coefficient distribution for the stationary NACA0012 airfoil at $\alpha = 0^\circ$ and $M_\infty = 0.8$.

considering a very large real time-step size in the implicit dual-time stepping method for the real time derivative term to be vanished, and then, marching in the pseudotime level until the error reaches a certain convergence criterion. Figure 10 shows the unstructured meshes (Mesh-I, Mesh-II, and Mesh-III with 1775, 3568, and 8552 quadrilateral cells, respectively) used to predict the flow field over the NACA0012 airfoil geometry. All the calculations performed in the present study for the stationary or moving NACA0012 airfoil are based on a small value of the relaxation time, i.e., $\tau = 0.001$, to reasonably simulate the inviscid flows.

The effect of the size of the computational mesh on the surface pressure coefficient distribution for the stationary NACA0012 airfoil is examined, as shown in Fig. 11. The study indicates that the shock is slightly predicted sharper by refining the mesh and Mesh-II and Mesh-III provide nearly the same results in both the shock region and the remaining part of the solution. Hereafter, Mesh-II and Mesh-III, referred to as the coarse and fine meshes, respectively, are used for the subsequent simulations and Mesh-I, given that it does

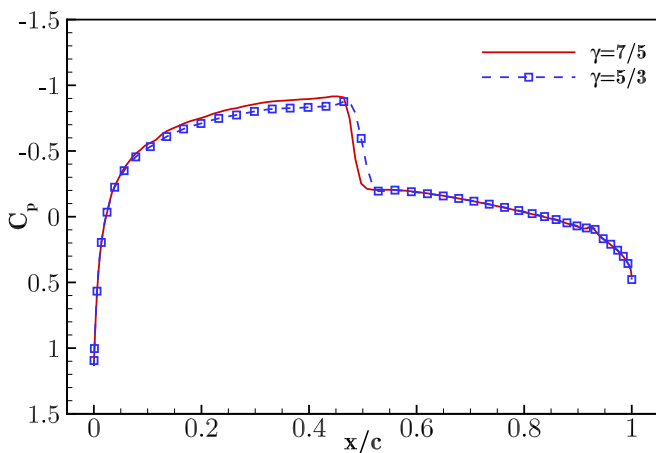


FIG. 14. Effect of value of specific-heat ratio on surface pressure coefficient distribution for the stationary NACA0012 airfoil at $\alpha = 0^\circ$ and $M_\infty = 0.8$.

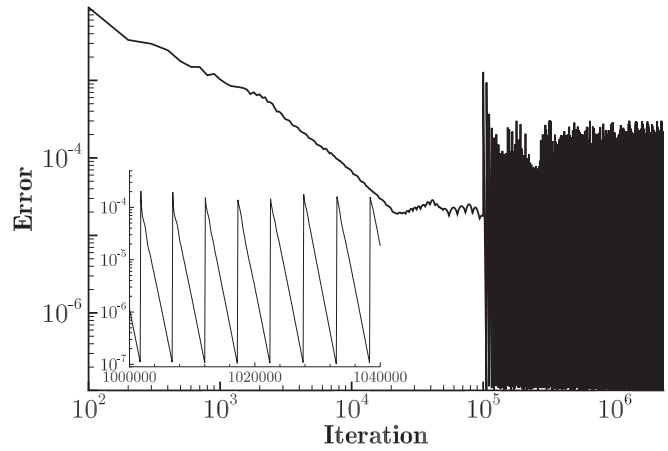


FIG. 15. Convergence history of the solution for the plunging NACA0012 airfoil.

not provide a desirable accuracy, will be disregarded. Note also that all the subsequent simulations for the stationary or moving NACA0012 airfoil are performed on the coarse mesh, unless otherwise indicated. To investigate the effect of the value of the second-order dissipation coefficient k_2 on the solution, this parameter is isolated by selecting a small value of the fourth-order dissipation coefficient, i.e., $k_4 = 0.0001$. Figure 12 indicates how this parameter affects the solution shown by the surface pressure coefficient distribution; increasing the value of k_2 will smear the shock wave as expected. On the other hand, the absence of this coefficient would not affect the stability of the solution algorithm for the condition considered here. Given the lower the values of k_2 the more accurate the results, $k_2 = 0$ seems a proper choice for the rest of the simulations. Figure 13 illustrates the effect of the value of the fourth-order dissipation coefficient k_4 on the solution. Increasing the value of k_4 will dissipate the solution expectedly, and therefore, a small amount, i.e., $k_4 = 0.0001$, is used for the subsequent simulations performed in this study. It is observed that the present solution obtained by applying the unstructured FVLBM is comparable with that of Davis and Bendiksen [38] which indicates the solution method adopted

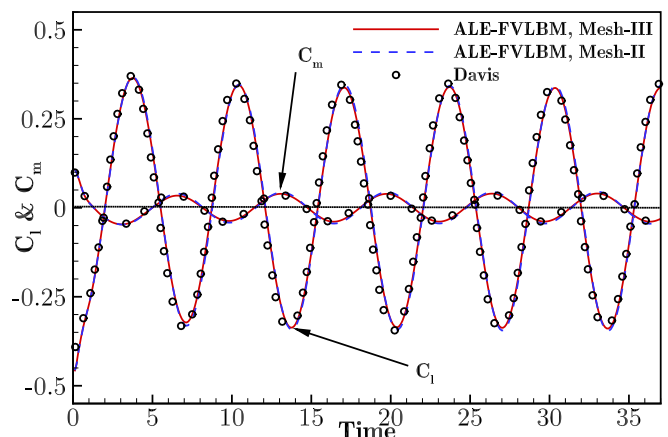


FIG. 16. Comparison of lift and moment coefficients vs nondimensional time for the plunging NACA0012 airfoil.

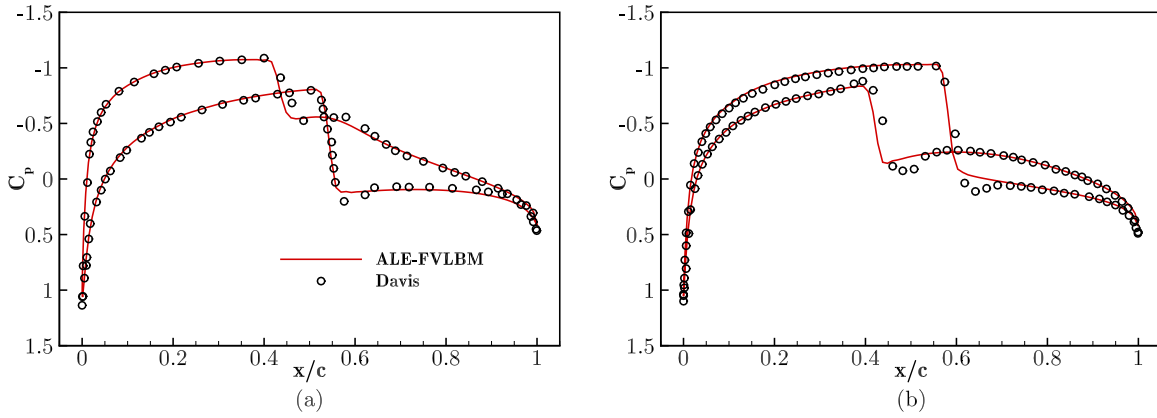


FIG. 17. Comparison of surface pressure coefficient distribution for the plunging NACA0012 airfoil during the upward motion at (a) $H = 0$ and (b) $H = H_{\max}$.

is suitable for computing the compressible inviscid flows with the shock in the flow domain.

Now, to study the effect of the value of the specific-heat ratios γ on the solution, the computations are carried out for both the diatomic and monatomic ideal gases, $\gamma = 7/5$ and $\gamma = 5/3$, and the corresponding surface pressure coefficient distributions for the stationary NACA0012 airfoil are given in Figure 14. It is indicated that a higher pressure on the airfoil surface before the shock region is predicted, the position of the shock is slightly shifted toward the trailing edge, and the strength of the shock is slightly decreased for the monatomic ideal gas $\gamma = 5/3$ compared to the diatomic case $\gamma = 7/5$.

D. Plunging NACA0012 airfoil

The next problem investigated is the forced vertical motion of the NACA0012 airfoil while its pitching angle is held constant at 0° . This test case was simulated by Davis and Bendiksen [38] by solving the Euler equations in the ALE framework and the present solution obtained by applying the ALE-FVLBM is compared with this reference. The vertical movement of the body is prescribed by

$$h(t) = H_{\max} \times \sin(\omega t), \tag{31}$$

where ω is the angular frequency of the oscillation which is related to the reduced frequency k as

$$k = \frac{\omega c}{2U_\infty}. \tag{32}$$

The maximum amplitude of the oscillation H_{\max} is set to be 0.1 of the airfoil chord length and the angular frequency of the motion ω is calculated from Eq. (32) by setting the reduced frequency to be $k = 0.5$. The freestream Mach number in this case is the same as that considered for the stationary test case, $M_\infty = 0.8$, and the present simulation is carried out on the coarse mesh as well as the fine mesh.

For initiating the unsteady solution, a steady-state solution is used by performing the simulation for the stationary airfoil and setting a reasonable convergence criterion, as indicated in the convergence history of the solution for the number of iterations to be about 10^5 in Figure 15. The convergence history of the unsteady-state solution performed by applying

the ALE-FVLBM is also demonstrated in Fig. 15 where the inner frame shows a random interval to clearly show the solution convergence in the pseudotime level for each real time step size. Figure 16 displays the lift and moment coefficients vs the nondimensional time obtained by applying the ALE FVLBM on both the coarse and fine meshes compared with the numerical results provided by Davis and Bendiksen which exhibit good agreement. It is also observed that the solution of

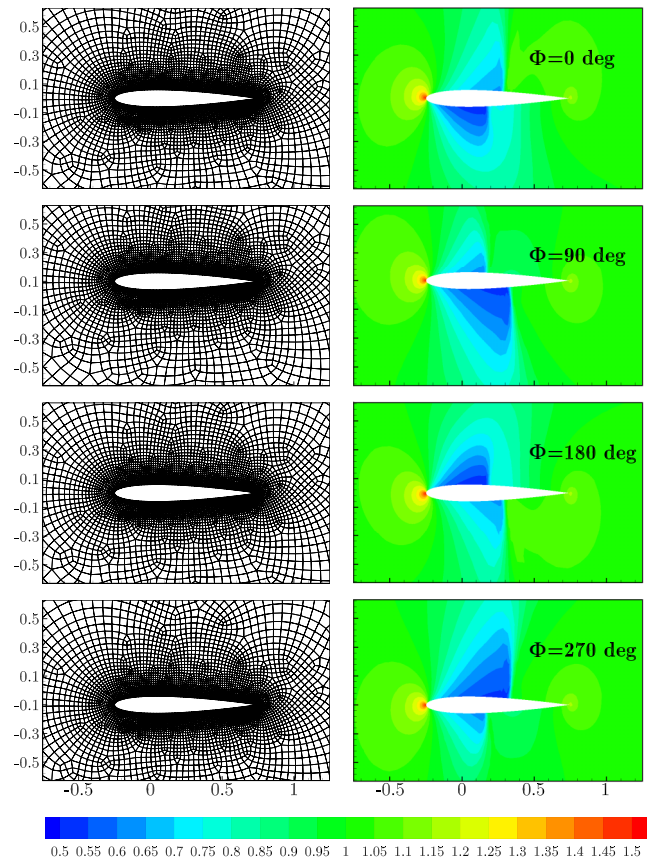


FIG. 18. Computed flow field shown by the pressure contours for the plunging NACA0012 airfoil at different vertical positions (right column) and their corresponding meshes (left column).

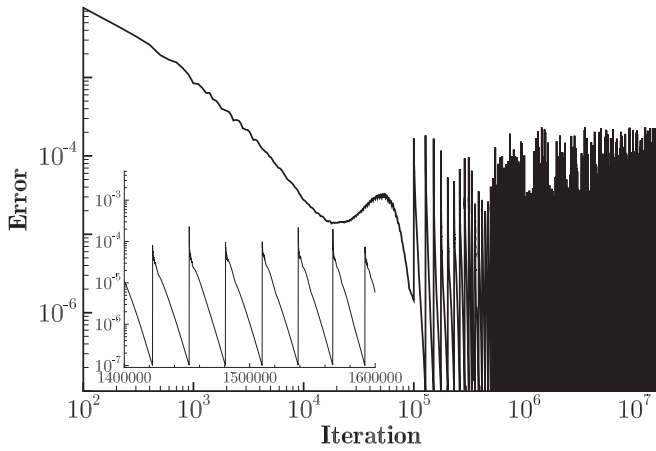


FIG. 19. Convergence history of the solution for the pitching NACA0012 airfoil (AGRAD CT5 test case).

the ALE-FVLBM for the coarse and fine meshes used here is almost the same. Figure 17 demonstrates that the surface pressure coefficient distribution predicted by the present solution is also comparable to the results of Davis *et al.* for the two instances of the motion, namely, at the zero vertical position during the up-stroke motion and at the maximum vertical

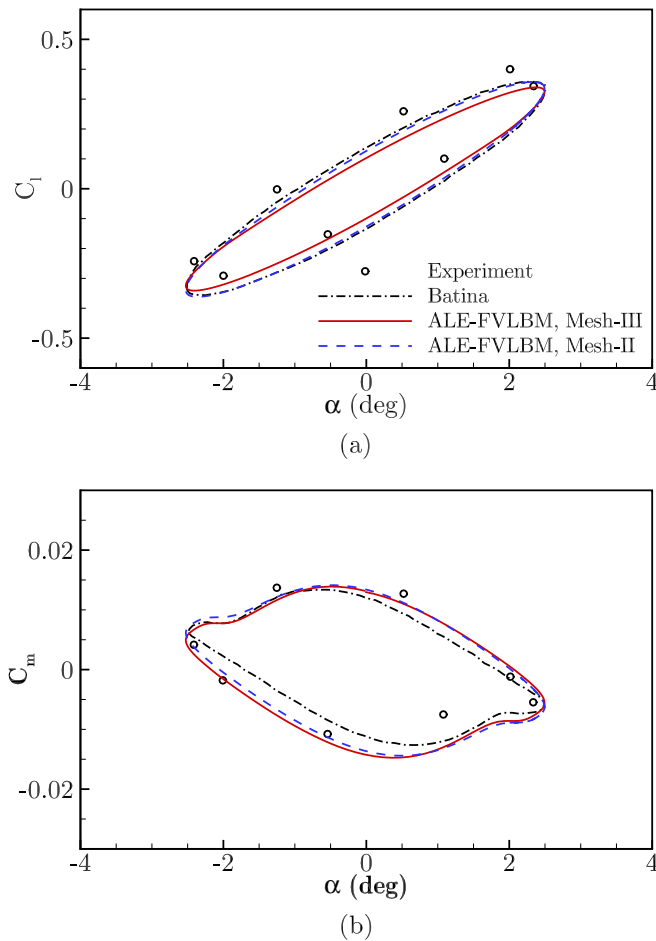


FIG. 20. Comparison of (a) lift and (b) moment coefficients vs angle of attack for the pitching NACA0012 airfoil (AGRAD CT5 test case).

position in the fourth cycle of the oscillation. The pressure contours and the unstructured meshes for the four different phases of the oscillation, $\Phi = 0^\circ, 90^\circ, 180^\circ,$ and 270° , are depicted in Fig. 18 clearly showing the formation and motion of the shock wave on the upper and lower surfaces of the airfoil. Note that the results presented in Figs. 17 and 18 are based on the fine mesh. It is found that the solution methodology presented here based on the unstructured finite-volume LBM in the ALE framework (ALE-FVLBM) is suitable for an accurate simulating the compressible inviscid flow over this moving geometry and the results obtained are comparable with those predicted by solving the Euler equations in the ALE framework.

E. Pitching NACA0012 airfoil

The next test case is the AGRAD CT case number 5 of Landon [57] (the AGRAD CT5 test case). In this test case, the NACA0012 airfoil experiences a forced sinusoidal rigid pitching motion while it is fixed in its vertical position. The freestream Mach number is $M_\infty = 0.755$ in which the airfoil experiences a transonic regime of the flow. The airfoil rotates around its quarter chord point $c/4$ with the pitch angle $\alpha(t)$

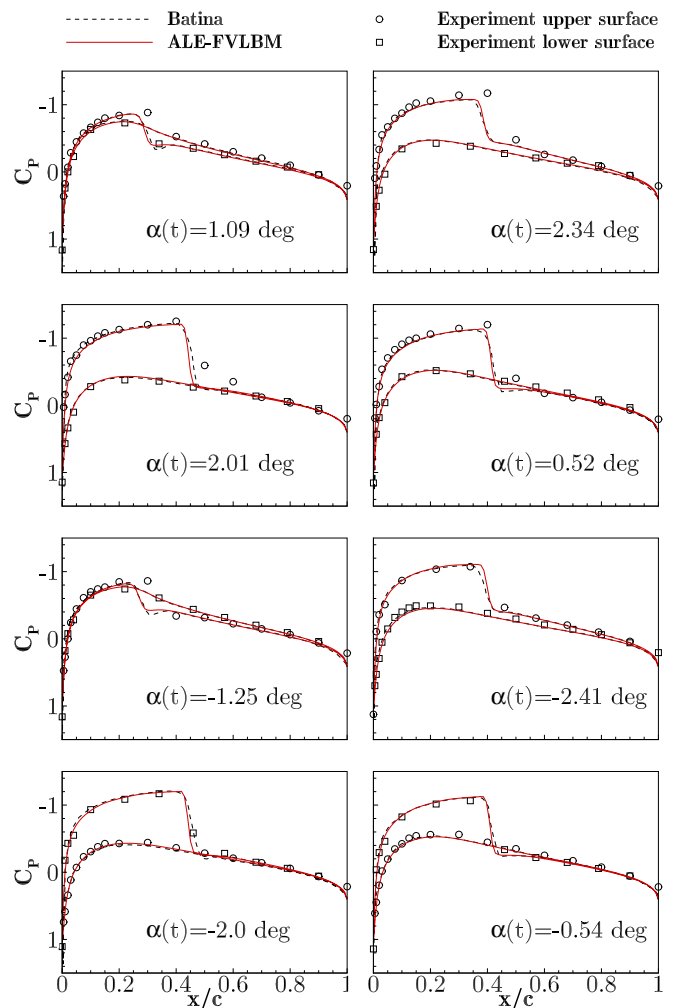


FIG. 21. Comparison of surface pressure coefficient distribution for the pitching NACA0012 airfoil at different angles of attack.

governed by

$$\alpha(t) = 0.016^\circ + 2.51^\circ \sin(\omega t), \quad (33)$$

where the angular frequency ω is obtained from Eq. (32) by setting the reduced frequency to be $k = 0.0814$, as considered for the AGARD CT5 test case [57].

For initiating the unsteady solution of the CT5 test case, a converged steady-state solution is used for the stationary airfoil. Note that the steady-state simulation is performed at the identical freestream condition to the CT5 test case. Figure 19 shows the convergence history of the solution for both the steady and unsteady conditions in which the inner frame shows a random interval to clearly show the solution convergence in the pseudotime level for each real time step size. The simulations are carried out on both the coarse and fine meshes to show the grid independency for this moving geometry. Figure 20 represents the variation of the lift and moment coefficients vs the pitching angle for the present simulation performed on both the coarse and fine meshes for a cycle of the airfoil motion and the results obtained by applying the ALE-FVLBM are comparable with the experimental data by Landon [57] and the numerical results by Batina [35]. It is observed that the unsteady solution obtained over the pitching NACA0012 airfoil is not very sensitive to the mesh sizes considered here. The predicted surface pressure coefficient distribution is also compared with the numerical results of

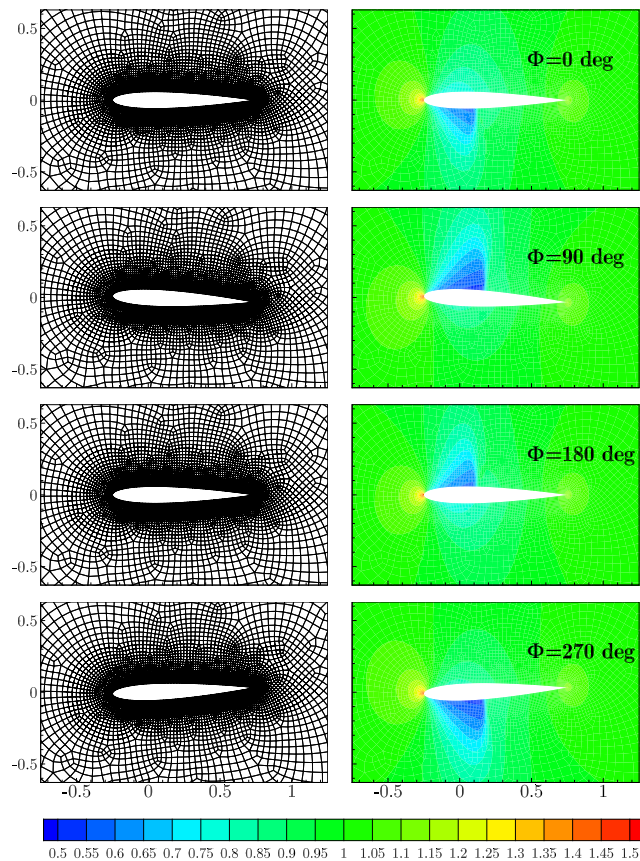


FIG. 22. Computed flow field shown by pressure contours for the pitching NACA0012 airfoil at different angles of attack (right column) and their corresponding meshes (left column).

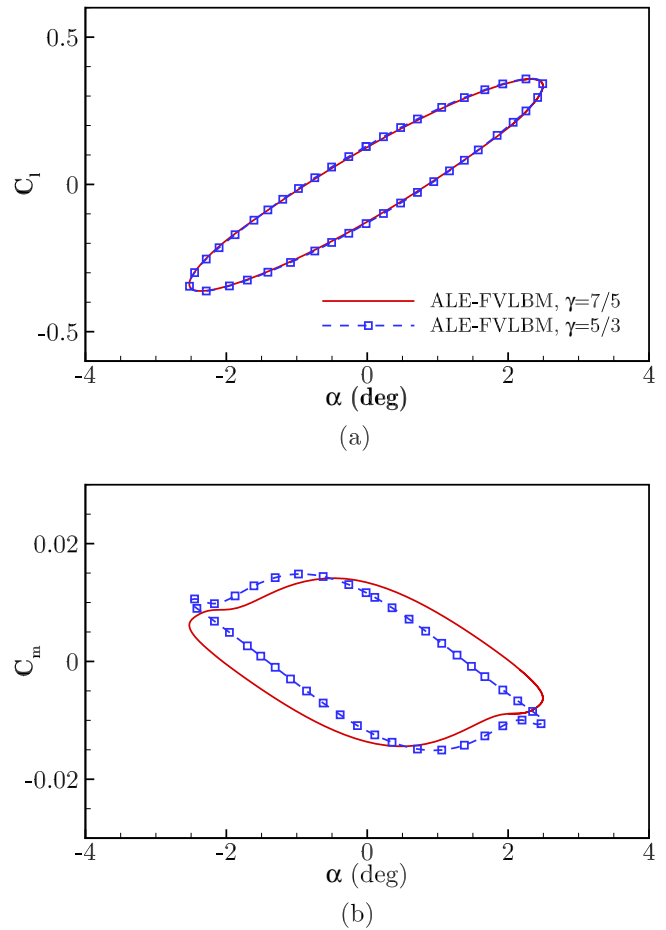


FIG. 23. Effect of value of specific-heat ratio on (a) lift and (b) moment coefficients vs angle of attack for the pitching NACA0012 airfoil.

Batina and the experimental data of Landon in eight different pitch angles, as shown in Fig. 21 and good agreement is observed. The four snapshots of the computed flow field shown by the pressure contours in a cycle of the motion are given in Fig. 22 together with their corresponding meshes and it is indicated that the shock wave at different positions on both the upper and lower surfaces is reasonably captured. Here, the fine mesh is used to obtain the results in Figs. 21 and 22. Note also that the present solution performed by applying the ALE-FVLBM provides the numerical results which are comparable with those of the ALE-FV Euler solver by Batina. Indications are that the ALE-FVLBM can be considered as an alternative to the ALE-FV Euler solvers for predicting the compressible inviscid flow over the moving bodies.

Figure 23 compares the variation of the lift and moment coefficients vs the pitching angle obtained by applying the ALE-FVLBM for the diatomic and monatomic ideal gases, $\gamma = 7/5$ and $\gamma = 5/3$. It is illustrated that the lift coefficient remains almost the same, however, the moment coefficient is changed significantly for these two ideal gases and this behavior is due to the change in the position of the shock formed on the surface of the airfoil, as also observed for the stationary NACA0012 airfoil.

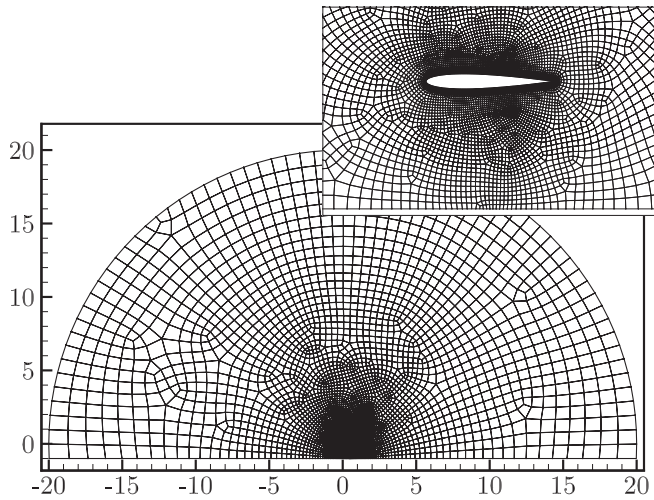


FIG. 24. Computational mesh for simulating the ground effect for the pitching NACA0012 airfoil.

F. Pitching or Plunging NACA0012 airfoil in the vicinity of the ground

The simulation of the flow for the oscillation of an airfoil in the vicinity of the ground is a practical and challenging problem and the use of an unstructured FV flow solver is a good choice for this aim. To perform an analysis for such a problem, the already simulated pitching or plunging airfoil is altered by adding a symmetry wall in the adjacent of the NACA0012 airfoil to replicate the effect of a flat ground. Figure 24 shows the computational unstructured mesh used to simulate the flow over the NACA0012 airfoil with the ground effect. The lower boundary of the domain is treated as a symmetric wall and the distance of the airfoil from the wall is equal to the chord of the airfoil. The other conditions involving in the problem are identical to the aforementioned ones in the pitching or plunging NACA0012 airfoil test cases.

The convergence history of the solution for the plunging NACA0012 airfoil in the vicinity of ground is presented in Fig. 25. The lift and moment coefficients vs the nondimensional time are illustrated in Fig. 26 with and without the

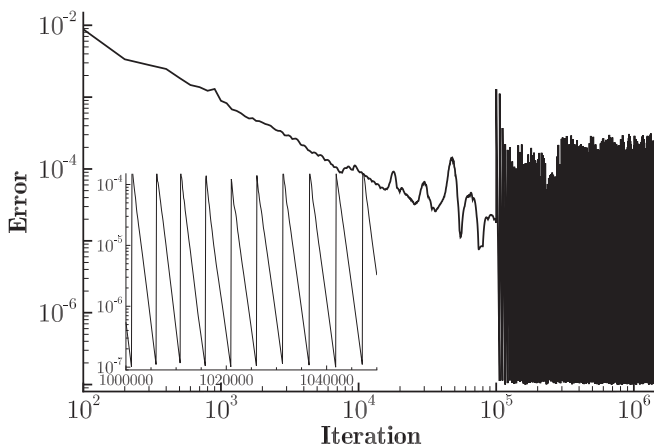


FIG. 25. Convergence history of the solution for the plunging NACA0012 airfoil with the ground effect.

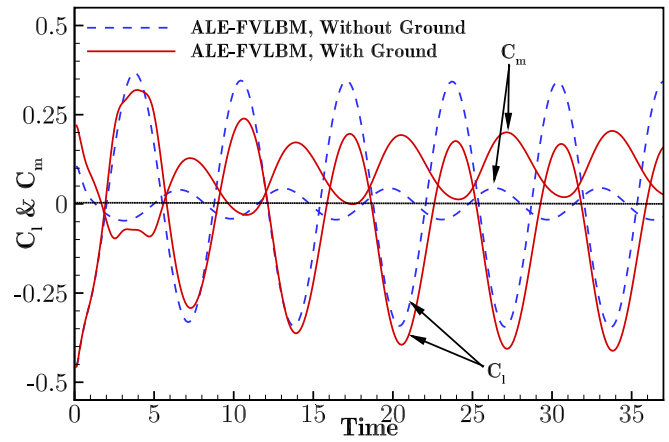


FIG. 26. Ground effect on lift and moment coefficients vs nondimensional time for the plunging NACA0012 airfoil.

ground effect. It is found that the ground has a considerable effect on the aerodynamic coefficients for this test case simulated. Figure 27 presents the flow field shown by the pressure contours and it is observed that the position and strength of the shock on both the upper and lower surfaces of the airfoil are changed due to the presence of the ground.

The convergence history of the solution for the pitching test case is plotted in Fig. 28 and it is observed that the solution is reasonably converged in the pseudotime level for each real time step size. The lift and moment coefficients vs the pitching angle for the CT5 test case with the ground effect are given in Fig. 29 and they are compared to the results without considering the ground. It is indicated that the aerodynamic coefficients for this moving airfoil are significantly changed with the ground effect for the flow conditions considered here. Figure 30 shows the pressure contours for the four phases of the motion and the effect of the ground in altering the flow field specifically on the shock wave formation is quite clear in this figure.

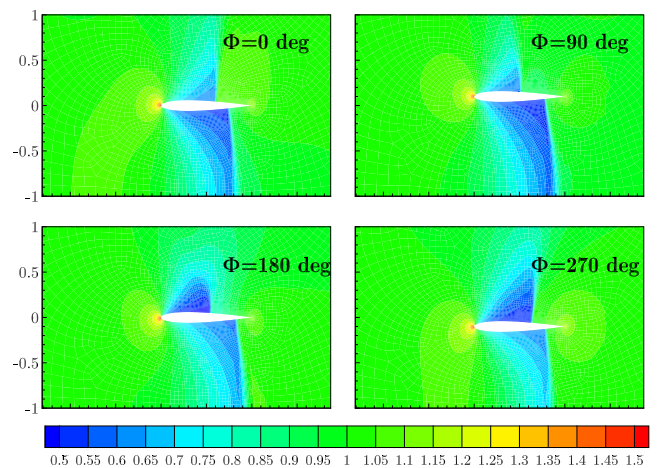


FIG. 27. Computed flow field shown by the pressure contours for the plunging NACA0012 airfoil in the vicinity of ground at different vertical positions.

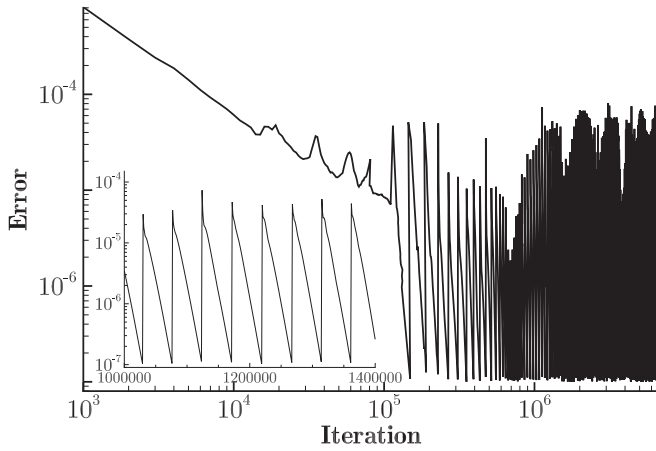
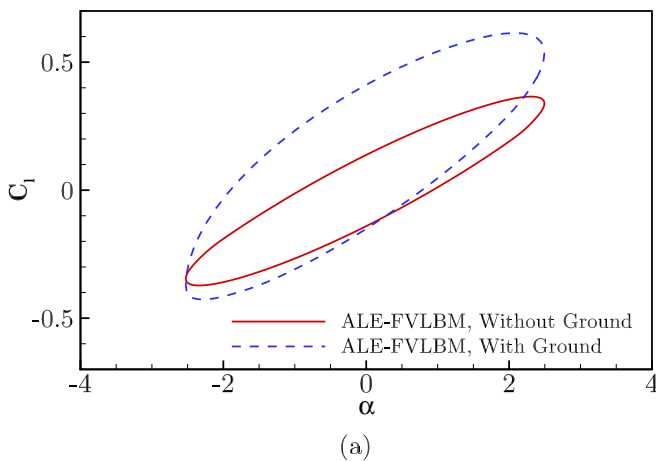


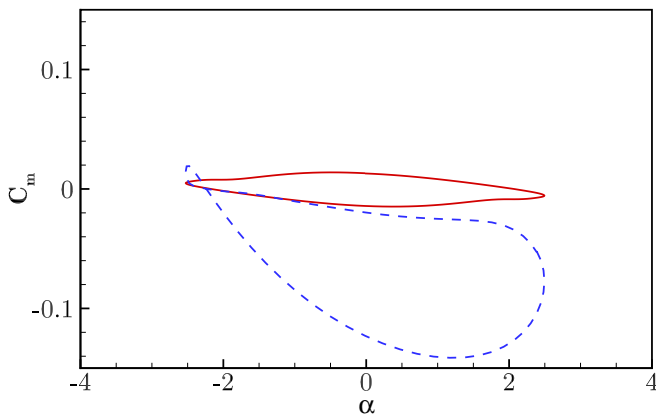
FIG. 28. Convergence history of the solution for the pitching NACA0012 airfoil with the ground effect.

V. CONCLUSION

In this study, an arbitrary Lagrangian-Eulerian unstructured finite-volume LBM (ALE-FVLBM) is developed and applied for the simulation of the compressible inviscid flows



(a)



(b)

FIG. 29. Ground effect on (a) lift and (b) moment coefficients vs angle of attack for the pitching NACA0012 airfoil.

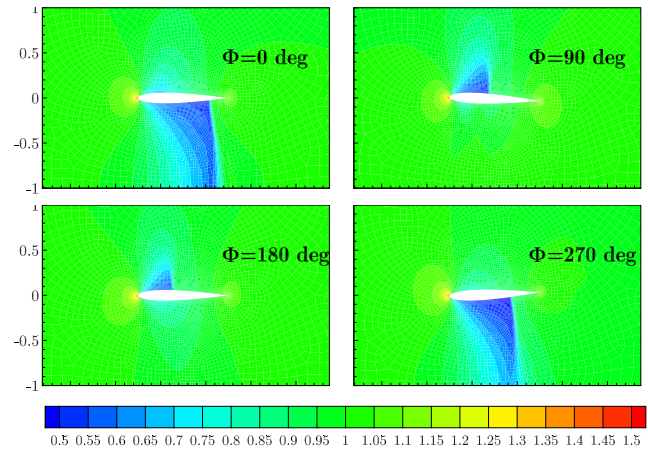


FIG. 30. Computed flow field shown by the pressure contours for the pitching NACA0012 airfoil in the vicinity of ground at different pitching angles.

over the moving bodies. For this aim, the compressible LB equation with the BGK approximation is formulated in the ALE framework and the resulting system of equations is discretized using a second-order cell-centered finite-volume method on the unstructured meshes. For the time integration, an implicit dual-time stepping method is utilized. Several test cases are simulated here to show the accuracy and robustness of the solution method adopted based on ALE-FVLBM. Some conclusions and remarks regarding the present study are as follows:

(1) The study shows that the solution methodology proposed based on the application of FVLBM is stable and robust for the simulation of the compressible inviscid flows over the stationary or moving bodies even with the discontinuities in the flow field such as shock waves. It is indicated that the computed results obtained by the present solution method are in good agreement with the available numerical and experimental results for the test cases considered.

(2) The solution methodology proposed based on the FVLBM formulated in the ALE framework on an unstructured body-fitted mesh can correctly model the body shape and properly admit the mesh movement owing to the body motion. Here, the finite-volume method is used for the solution of the compressible LB equation in the ALE framework, however, the solution procedure introduced here can be applied to other numerical approaches.

(3) The moving airfoil near the ground is successfully simulated as a practical and challenging problem to further show the applicability of the present solution method to deal with complex physics. It is shown that the solution methodology proposed based on the ALE-FVLBM is capable of accurately computing the compressible inviscid flows around the moving bodies with and without the ground effect. The use of the unstructured meshes in the ALE-FVLBM enhances the solution method adopted here to handle practical and complicated problems.

(4) Here, the multiple particle speed LB model proposed by Watari is incorporated in the ALE-FVLBM to correctly model the compressibility effects. The proposed solution

method with this LB model has the capability of computing the compressible flows with different values of the specific-heat ratios, as demonstrated here by simulating both the stationary and moving bodies. Note that the use of other LB models in the solution method proposed here is straightforward to perform.

(5) It is indicated that the results obtained by the ALE-FVLBM for the compressible inviscid flows over the moving bodies follow the results of the ALE-FV Euler solvers carried out by other researchers. The ALE-FVLBM has a simpler formulation, and thus, it can be considered as an alternative to the traditional solution methods, namely the ALE-FV Euler

solvers. Note that the LBM with a unified formulation and by some modifications to incorporate the no-slip boundary conditions can be used to compute the viscous effects. Thus, the ALE-FVLBM proposed here can be further extended to be used for the simulation of the compressible viscous flows over the moving bodies.

ACKNOWLEDGMENTS

The authors would like to acknowledge Sharif University of Technology for the support of this work.

-
- [1] S. Succi, *The Lattice Boltzmann Equation: For Fluid Dynamics and Beyond* (Oxford University Press, New York, 2001).
 - [2] P. L. Bhatnagar, E. P. Gross, and M. Krook, A model for collision processes in gases. I. small amplitude processes in charged and neutral one-component systems, *Phys. Rev.* **94**, 511 (1954).
 - [3] R. M. C. So, S. C. Fu, and R. C. K. Leung, Finite difference lattice Boltzmann method for compressible thermal fluids, *AIAA J.* **48**, 1059 (2010).
 - [4] K. Hejranfar and E. Ezzatneshan, A high-order compact finite-difference lattice Boltzmann method for simulation of steady and unsteady incompressible flows, *Int. J. Numer. Methods Fluids* **75**, 713 (2014).
 - [5] K. Hejranfar and E. Ezzatneshan, Implementation of a high-order compact finite-difference lattice Boltzmann method in generalized curvilinear coordinates, *J. Comput. Phys.* **267**, 28 (2014).
 - [6] M. Watari and M. Tsutahara, Supersonic flow simulations by a three-dimensional multispeed thermal model of the finite difference lattice Boltzmann method, *Physica A* **364**, 129 (2006).
 - [7] M. Watari, Finite difference lattice Boltzmann method with arbitrary specific heat ratio applicable to supersonic flow simulations, *Physica A* **382**, 502 (2007).
 - [8] K. Hejranfar and M. H. Saadat, Preconditioned WENO finite-difference lattice Boltzmann method for simulation of incompressible turbulent flows, *Comput. Math. Appl.* **76**, 1427 (2018).
 - [9] K. Hejranfar, M. H. Saadat, and S. Taheri, High-order weighted essentially nonoscillatory finite-difference formulation of the lattice Boltzmann method in generalized curvilinear coordinates, *Phys. Rev. E* **95**, 023314 (2017).
 - [10] D. V. Patil and K. N. Lakshmisha, Finite volume TVD formulation of lattice Boltzmann simulation on unstructured mesh, *J. Comput. Phys.* **228**, 5262 (2009).
 - [11] N. Rossi, S. Ubertini, G. Bella, and S. Succi, Unstructured lattice Boltzmann method in three dimensions, *Int. J. Numer. Methods Fluids* **49**, 619 (2005).
 - [12] S. Ubertini and S. Succi, A generalised lattice Boltzmann equation on unstructured grids, *Commun. Comput. Phys.* **3**, 342 (2008).
 - [13] A. Karbalaeei and K. Hejranfar, A Central Difference Finite Volume Lattice Boltzmann Method for Simulation of 2D Inviscid Compressible Flows on Triangular Meshes, in *Proceedings of the ASME 2018 International Mechanical Engineering Congress and Exposition. Volume 7: Fluids Engineering November 9–15, 2018, Pittsburgh, Pennsylvania, USA* (ASME, 2019).
 - [14] S. Geller, M. Krafczyk, J. Tölke, S. Turek, and J. Hron, Benchmark computations based on lattice-Boltzmann, finite element and finite volume methods for laminar flows, *Comput. Fluids* **35**, 888 (2006).
 - [15] K. C. Uga, M. Min, T. Lee, and P. F. Fischer, Spectral-element discontinuous Galerkin lattice Boltzmann simulation of flow past two cylinders in tandem with an exponential time integrator, *Comput. Math. Appl.* **65**, 239 (2013).
 - [16] A. Zadehgo, M. Ashrafizaadeh, and S. H. Musavi, A nodal discontinuous Galerkin lattice Boltzmann method for fluid flow problems, *Comput. Fluids* **105**, 58 (2014).
 - [17] K. Hejranfar and M. Hajihassanpour, Chebyshev collocation spectral lattice Boltzmann method for simulation of low-speed flows, *Phys. Rev. E* **91**, 013301 (2015).
 - [18] K. Hejranfar and M. Hajihassanpour, Chebyshev collocation spectral lattice Boltzmann method in generalized curvilinear coordinates, *Comput. Fluids* **146**, 154 (2017).
 - [19] K. Hejranfar and A. Ghaffarian, A spectral difference lattice Boltzmann method for solution of inviscid compressible flows on structured grids, *Comput. Math. Appl.* **72**, 1341 (2016).
 - [20] A. Ghaffarian and K. Hejranfar, An implicit dual-time stepping spectral difference lattice Boltzmann method for simulation of viscous compressible flows on structured meshes, *Meccanica* **54**, 1561 (2019).
 - [21] Z.-G. Feng and E. E. Michaelides, The immersed boundary-lattice Boltzmann method for solving fluid-particles interaction problems, *J. Comput. Phys.* **195**, 602 (2004).
 - [22] C. Shu, N. Liu, and Y. T. Chew, A novel immersed boundary velocity correction-lattice Boltzmann method and its application to simulate flow past a circular cylinder, *J. Comput. Phys.* **226**, 1607 (2007).
 - [23] Y. Sui, Y. T. Chew, P. Roy, and H. T. Low, A hybrid method to study flow-induced deformation of three-dimensional capsules, *J. Comput. Phys.* **227**, 6351 (2008).
 - [24] J. Wu and C. Shu, An improved immersed boundary-lattice Boltzmann method for simulating three-dimensional incompressible flows, *J. Comput. Phys.* **229**, 5022 (2010).
 - [25] T. Inamuro, Lattice Boltzmann methods for moving boundary flows, *Fluid Dyn. Res.* **44**, 024001 (2012).
 - [26] P. Lallemand and L.-S. Luo, Lattice Boltzmann method for moving boundaries, *J. Comput. Phys.* **184**, 406 (2003).

- [27] D. Yu, R. Mei, L.-S. Luo, and W. Shyy, Viscous flow computations with the method of lattice Boltzmann equation, *Prog. Aerosp. Sci.* **39**, 329 (2003).
- [28] Z. Xia, K. W. Connington, S. Rapaka, P. Yue, J. J. Feng, and S. Chen, Flow patterns in the sedimentation of an elliptical particle, *J. Fluid Mech.* **625**, 249 (2009).
- [29] B. Dorschner, S. S. Chikatamarla, and I. V. Karlin, Entropic multirelaxation-time lattice Boltzmann method for moving and deforming geometries in three dimensions, *Phys. Rev. E* **95**, 063306 (2017).
- [30] B. Dorschner, S. S. Chikatamarla, F. Bösch, and I. V. Karlin, Grad's approximation for moving and stationary walls in entropic lattice Boltzmann simulations, *J. Comput. Phys.* **295**, 340 (2015).
- [31] G. Di Ilio, D. Chiappini, S. Ubertini, G. Bella, and S. Succi, Hybrid lattice Boltzmann method on overlapping grids, *Phys. Rev. E* **95**, 013309 (2017).
- [32] G. Di Ilio, D. Chiappini, S. Ubertini, G. Bella, and S. Succi, Fluid flow around NACA 0012 airfoil at low-Reynolds numbers with hybrid lattice Boltzmann method, *Comput. Fluids* **166**, 200, (2018).
- [33] G. Di Ilio, D. Chiappini, S. Ubertini, G. Bella, and S. Succi, A moving-grid approach for fluid–structure interaction problems with hybrid lattice Boltzmann method, *Comput. Phys. Commun.* **234**, 137, (2019).
- [34] M. Meldi, E. Vergnault, and P. Sagaut, An arbitrary Lagrangian–Eulerian approach for the simulation of immersed moving solids with Lattice Boltzmann Method, *J. Comput. Phys.* **235**, 182, (2013).
- [35] J. T. Batina, Unsteady Euler airfoil solutions using unstructured dynamic meshes, *AIAA J.* **28**, 1381 (1990).
- [36] S. M. Mirsajedi, S. M. H. Karimian, and M. Mani, A multizone moving mesh algorithm for simulation of flow around a rigid body with arbitrary motion, *J. Fluids Eng.* **128**, 297 (2005).
- [37] R. Sevilla, A. J. Gil, and M. Weberstadt, A high-order stabilised ALE finite element formulation for the Euler equations on deformable domains, *Comput. Struct.* **181**, 89 (2017).
- [38] G. A. Davis and O. O. Bendiksen, Unsteady transonic two-dimensional Euler solutions using finite elements, *AIAA J.* **31**, 1051 (1993).
- [39] K. Hejranfar and M. H. Azampour, Simulation of 2D fluid–structure interaction in inviscid compressible flows using a cell-vertex central difference finite volume method, *J. Fluids Struct.* **67**, 190 (2016).
- [40] F. J. Alexander, H. Chen, S. Chen, and G. D. Doolen, Lattice Boltzmann model for compressible fluids, *Phys. Rev. A* **46**, 1967 (1992).
- [41] H. Yu and K. Zhao, Lattice Boltzmann method for compressible flows with high Mach numbers, *Phys. Rev. E* **61**, 3867 (2000).
- [42] F. L. Hinton, M. N. Rosenbluth, S. K. Wong, Y. R. Lin-Liu, and R. L. Miller, Modified Lattice Boltzmann method for compressible fluid simulations, *Phys. Rev. E* **63**, 061212, (2001).
- [43] C. Sun and A. T. Hsu, Three-dimensional lattice Boltzmann model for compressible flows, *Phys. Rev. E* **68**, 016303 (2003).
- [44] T. Kataoka and M. Tsutahara, Lattice Boltzmann model for the compressible Navier-Stokes equations with flexible specific-heat ratio, *Phys. Rev. E* **69**, 035701(R) (2004).
- [45] T. Kataoka and M. Tsutahara, Lattice Boltzmann method for the compressible Euler equations, *Phys. Rev. E* **69**, 056702 (2004).
- [46] P. C. Philippi, L. A. Hegele, L. O. E. dos Santos, and R. Surmas, From the continuous to the lattice Boltzmann equation: The discretization problem and thermal models, *Phys. Rev. E* **73**, 056702 (2006).
- [47] S. S. Chikatamarla and I. V. Karlin, Lattices for the lattice Boltzmann method, *Phys. Rev. E* **79**, 046701 (2009).
- [48] M. Sbragaglia, R. Benzi, L. Biferale, H. Chen, X. Shan, and S. Succi, Lattice Boltzmann method with self-consistent thermohydrodynamic equilibria, *J. Fluid Mech.* **628**, 299 (2009).
- [49] N. Frapolli, S. S. Chikatamarla, and I. V. Karlin, Multispeed entropic lattice Boltzmann model for thermal flows, *Phys. Rev. E* **90**, 043306 (2014).
- [50] M. Atif, M. Namburi, and S. Ansumali, Higher-order lattice Boltzmann model for thermohydrodynamics, *Phys. Rev. E* **98**, 053311, (2018).
- [51] M. H. Saadat, F. Bösch, and I. V. Karlin, Lattice Boltzmann model for compressible flows on standard lattices: Variable Prandtl number and adiabatic exponent, *Phys. Rev. E* **99**, 013306 (2019).
- [52] A. Jameson, W. Schmidt, and Eli Turkel, Numerical solution of the Euler equations by finite volume methods using Runge Kutta time stepping schemes, in *14th Fluid and Plasma Dynamics Conference 23-25 June, 1981, Palo Alto, CA, USA* (AIAA, 2012).
- [53] W. K. Anderson, A grid generation and flow solution method for the Euler equations on unstructured grids, *J. Comput. Phys.* **110**, 23 (1994).
- [54] C. Farhat, C. Degand, B. Koobus, and M. Lesoinne, Torsional springs for two-dimensional dynamic unstructured fluid meshes, *Comput. Methods Appl. Mech. Eng.* **163**, 231 (1998).
- [55] P. D. Thomas and C. K. Lombard, Geometric conservation law and its application to flow computations on moving grids, *AIAA J.* **17**, 1030 (1979).
- [56] K. Ou and A. Jameson, On the temporal and spatial accuracy of spectral difference method on moving deformable grids and the effect of geometric conservation law, in *40th Fluid Dynamics Conference and Exhibit 28 June - 01 July, 2010, Chicago, Illinois* (AIAA, 2012).
- [57] R. Landon, NACA 0012 oscillating and transient pitching, Compendium of unsteady aerodynamic measurements, Data Set 3 in AGARD Report No. 702, 1982, pp. 3.1-3.25